PCCP

Computational Study of the Rovibrational Spectrum of CO2–N2

Journal:	*Physical Chemistry Chemical Physics*
Manuscript ID	CP-ART-08-2020-004186.R1
Article Type:	Paper
Date Submitted by the Author:	02-Sep-2020
Complete List of Authors:	Quintas-Sánchez, Ernesto; Missouri University of Science and Technology, Chemistry Dawes, Richard; Missouri University of Science and Technology, Chemistry Wang, Xiao-Gang; Queen's University, Chemistry Carrington, Tucker; Queen's University,

Journal Name

ARTICLE TYPE

Cite this: DOI: 10.1039/xxxxxxxxxx

Computational Study of the Rovibrational Spectrum of CO_2–N_2

E. Quintas-Sánchez,[a] R. Dawes,*[a] Xiao-Gang Wang,[b] Tucker Carrington Jr.*[b]

Received Date
Accepted Date

DOI: 10.1039/xxxxxxxxxx

www.rsc.org/journalname

The CO_2–N_2 complex is formed from two key components of Earth's atmosphere, and as such, has received some attention from both experimental and theoretical studies. On the theory side, a potential energy surface (PES) based on high level *ab initio* data was reported [Nasri *et al.*, J. Chem. Phys., 2015, **142**, 174301] and then used in more recently reported rovibrational calculations [Lara-Moreno *et al.*, Phys. Chem. Chem. Phys., 2019, **21**, 3550]. Accuracy of about 1 percent was achieved for calculated rotational transitions of the ground vibrational state of the complex, compared with previously reported microwave spectra. However, a very recent measurement of the geared bending mode frequency [Barclay *et al.*, J. Chem. Phys., 2020, **153**, 014303] recorded a value of 21.4 cm^{-1}, which is wildly different from the corresponding calculated value of 45.9 cm^{-1}. To provide some insight into this discrepancy, we have constructed a new more accurate PES, and used it to perform highly converged variational rovibrational calculations. Our new results yield a value of 21.1 cm^{-1} for that bending frequency, in close agreement with the experiment. We also obtain significantly improved predicted rotational transitions. Finally, we note that a very shallow well, previously reported as a distinct second isomer, is not found on our new PES, but rather a transition structure is seen in that location.

1 Introduction

Computational prediction of the rovibrational spectra of Van der Waals (vdW) complexes has become reliable and sufficiently accurate so as to guide experiments and aid in their assignment. Despite the challenges associated with the commonly occurring floppiness and possibly multi-welled nature of the potential energy surface (PES), especially for complexes of small closed-shell monomers, it is generally straightforward (at least for rigid monomers) to construct an accurate PES and solve for the bound rovibrational states—thus yielding insight into measurable spectroscopic transitions. We have performed many such studies, combining automated PES-fitting with a highly converged variational approach to solve the Hamiltonian for the nuclei. Examples include $(OCS)_2$,[1] $(CO)_2$,[2] $(CO_2)_2$,[3] CO_2–CO,[4] CO_2–CS_2,[5] $(NNO)_2$,[6] CO_2–HCCH,[7] O_2–CO,[8] O_3–Ar,[9] CO–N_2,[10] CS–Ar and SiS–Ar.[11] In each case, guided by our automated fitting algorithm, electronic energies were computed using coupled-cluster theory—usually either CCSD(T) or the explicitly-correlated variant CCSD(T)-F12b—combined with large basis sets, often extrapolated towards the complete basis set (CBS) limit. The geometries needed to define an accurate fitted PES are determined and the electronic-structure data is computed automatically by our fitting program AUTOSURF.[12] The details of this procedure have been described previously. Once an accurate PES has been constructed, it is interfaced to a variational rovibrational code called RV4.[6,13] RV4 is a parallel implementation of a variational method called DSL[14–16] which uses a product basis with discrete variable representation (DVR) functions (D)[17,18] for the stretches and spherical harmonic type functions (S) for the

[a] *Missouri University of Science and Technology, Rolla, MO 65409-0010, USA. Email: dawesr@mst.edu, quintassancheze@mst.edu*
[b] *Chemistry Department, Queen's University, Kingston, Ontario K7L 3N6, Canada. Email: tucker.tarrington@queensu.ca, xgwang.dalian@gmail.com*

bends[14,15,19,20] and a symmetry-adapted Lanczos eigensolver (L). The bend basis is appropriate for dealing with large amplitude bending motions. The symmetry-adapted iterative Lanczos-based eigensolver permits the use of generously large basis sets, ensuring strict convergence (without prohibitively large computer memory requirements) and without introducing basis size reduction techniques such as basis pruning or contraction. Symmetry, parity, and angular momentum quantum numbers can all be specified, and wavefunction and probability density plotting are available, as well as some additional analysis tools such as vibrational parent analysis. These methods and capabilities have been described in detail elsewhere.[3,4,7]

For a complex such as CO_2–N_2, composed of two linear monomers, there are four intermolecular coordinates, and so within the generally excellent approximation of rigid monomers, the PES and vibrational Hamiltonian are four dimensional (4D). In 4D, using our methods, it is typically possible to fit the PES to sub-cm^{-1} accuracy with about 2000 data points—depending on symmetry, topography, energy range, etc. In 4D, it is also typically possible to converge the low-lying rovibrational levels on a given PES to better than 0.001 cm^{-1} using a product basis of a few million functions. This means that it is thereby possible to obtain the rovibrational levels that directly reflect the underlying level of electronic structure theory used to construct the PES, and therefore it is simply a matter of selecting a sufficiently accurate electronic structure method, assuming that it is affordable. Following this procedure, highly accurate results were obtained for all of the example systems listed above. No serious anomalies were noted in any system, and errors below 1 cm^{-1} for vdW mode frequencies, and a few MHz for rotational transitions are typical—especially when CBS extrapolation was employed in the electronic structure protocol.

Nevertheless, a surprisingly large discrepancy recently came to light. A computational study by Lara-Moreno *et al.*[21] reporting rovibrational levels for the CO_2–N_2 complex, computed using a variational method and a high-level PES,[22] disagree wildly with new experimental measurements. The ν_g vdW geared bending-mode frequency was calculated at 45.9 cm^{-1}, and measured at 21.4 cm^{-1}.[23] The experiment actually measured combination bands with CO_2 excited in the asymmetric stretch, ν_3. Due to weak coupling with intermolecular modes, differences between the so extracted vdW levels, and the actual ground state frequencies are typically on the order of 0.1 cm^{-1}.[11,24] Several explanations for the discrepancy seem possible. On the experimental side, it is possible that the measured transition was incorrectly analyzed or miss-assigned. On the theory side, there are several possibilities. It is possible that there are serious errors in the fitted PES, or that there are bugs or errors in the vibrational code. It is also possible that the rovibrational calculations are not well-enough converged. The electronic structure method employed in the theoretical study could be slightly improved, but is of high-enough level to be generally reliable. The reported vibrational calculations necessarily employed a procedure of basis truncation and contraction, since they did not make use of an iterative solver. Indeed, although apparently showing indications of convergence, the reported primitive basis is substantially smaller than what we typically use in our calculations. Hereafter, we will refer to the previously reported rovibrational results by Lara-Moreno *et al.*[21] as LSHH. Another PES for this system was reported in 2018 by Crusius *et al.*,[25] based on MP2 theory with some CCSD(T)-based corrections, but they didn't compute rovibrational levels.

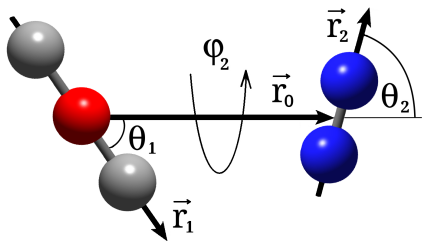

Fig. 1 Coordinates used to describe the CO_2–N_2 interaction. r_0: center-of-mass separation (length of $\vec{r}_0$). θ_1 and θ_2: angles between $\vec{r}_0$ and vectors $\vec{r}_1$ and $\vec{r}_2$. φ_2: torsional angle.

To hopefully resolve the discrepancy, we have computed a new more accurate PES, and used it compute highly converged rovibrational levels. In section 2 we describe the electronic structure protocol and fitting procedure, also characterizing the PES. In section 3, we describe the rovibrational calculations. In section 4 we provide results, analysis, and discussions, followed by a summary and conclusions.

2 Potential energy surface

The coordinates used to define the 4D CO_2–N_2 PES are the Jacobi coordinates: r_0, θ_1, θ_2, and φ_2, depicted in Fig. 1. As shown in the figure, $\vec{r}_0$ is the vector between the center-of-mass of the two fragments, and $\vec{r}_1$ and $\vec{r}_2$ are vectors aligned with the bond axes of the fragments ($\vec{r}_1$ for CO_2 and $\vec{r}_2$ for N_2), used here only to define the angles θ_1 and θ_2. Coordinate r_0 is the length of vector $\vec{r}_0$, while coordinates θ_1 and θ_2 correspond (respectively) to the angles between $\vec{r}_0$ and the vectors $\vec{r}_1$ and $\vec{r}_2$. The fourth coordinate is the dihedral (out of plane) torsional angle, labeled φ_2, which is the angle between the vectors $\vec{r}_0 \times \vec{r}_1$ and $\vec{r}_0 \times \vec{r}_2$.

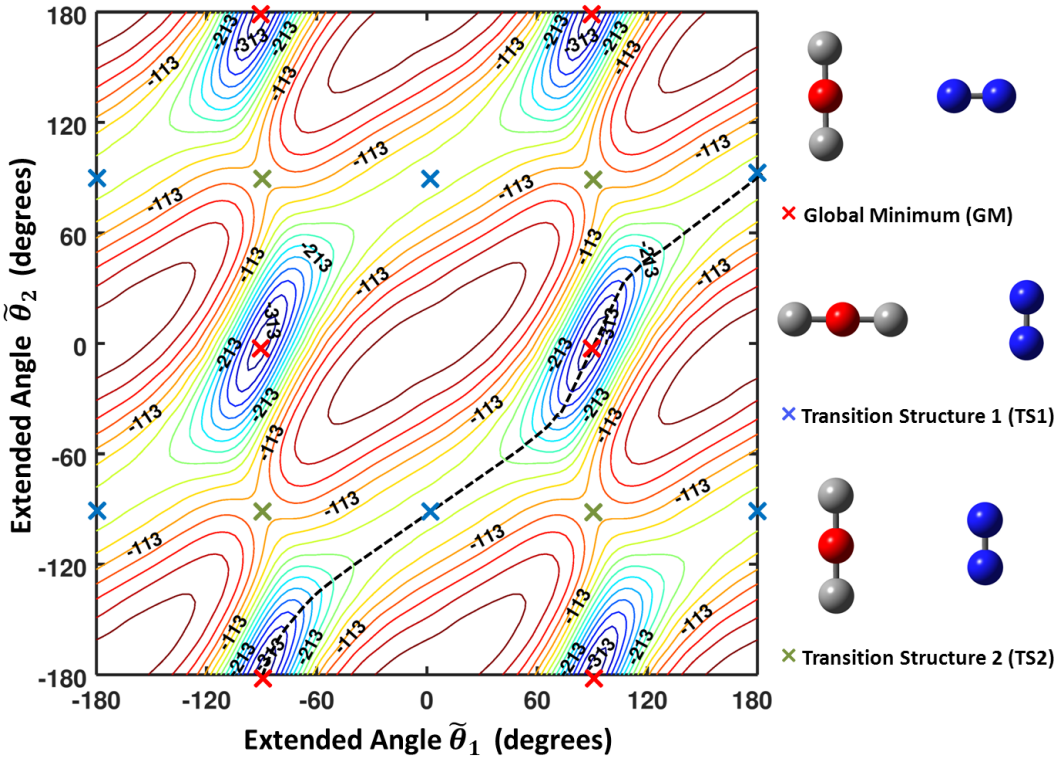

Fig. 2 r_0-optimized contour plot of the PES as a function of the extended angles $\tilde{\theta}_1$ and $\tilde{\theta}_2$. For each pair of angles, the energy (given in cm^{-1}) is optimized with respect to the center-of-mass distance r_0. The position of each stationary point—and the corresponding molecular configuration—is also highlighted. The dashed line represents the disrotatory energy path connecting equivalent minima.

2.1 Electronic structure calculations

In this study, both monomers are approximated as rigid, held at their ground state vibrationally-averaged structures. It is a good approximation in this application to consider only the inter-monomer coordinates because their frequencies are all much less than those of the intra-monomer coordinates. The CO_2 molecule is held linear, with each CO bond-distance fixed at 1.162086 Å,[26] which is consistent with the experimental rotational constant $B = 0.39022$ cm^{-1}.[27,28] The NN bond length is fixed at 1.0975 Å, consistent with its rotational constant of $B = 1.98950$ cm^{-1}.[29] All *ab initio* calculations were performed using the MOLPRO electronic structure code package.[30]

The final high-level PES was constructed using *ab initio* data computed with explicitly-correlated coupled-cluster theory.[31] The complete basis set limit was estimated by extrapolating calculations at the CCSD(T)-F12b/VTZ-F12 and CCSD(T)-F12b/VQZ-F12 levels, using the l^{-3} formula.[32] As discussed below, a lower-level guide surface (to avoid computing high level data at inaccessible geometries) was also constructed; this was done using data at the CCSD(T)-F12a/VDZ-F12 level of theory.

2.2 Analytical representation

As we have done in the past for other vdW linear dimers,[1–8,33,34] the 4D PES analytical representation was constructed using an automated interpolating moving least-squares methodology, which has been recently released as a software package under the name AUTOSURF.[12] As usual,[35] a local fit was expanded about each data point, and the final potential is obtained as the normalized weighted sum of the local fits. This interpolative approach can accommodate arbitrary energy-surface topographies and is particularly advantageous in cases of PESs with large anisotropy, which are challenging for traditional quadrature-type expansions. The procedure has been described in detail elsewhere.[6,12,36]

The short range part of the PES is restricted by excluding regions with repulsive energies above a maximum of 6 kcal/mol (~ 2100 cm^{-1}) relative to the separated monomers asymptote. The fitted range of the PES extends only to $r_0 = 15.0$ Å for this spectroscopic application, while the zero of energy is set at infinite center-of-mass separation between the monomers. For each of the local fits, a fitting basis of 301 functions is used. As has been previously described,[35] our default fitting basis is a product of radial functions and angular functions (associated Legendre poly-

nomials with a cosine-based torsional function). The radial function is designed to accommodate the slowly varying long range appropriate for neutral–neutral quadrupole–quadrupole interactions, while avoiding unnecessary flexibility that could allow oscillations. The maximum value of the Legendre l, and cosine m indices used in the interpolative fitting basis is $l_{max} = 6$, $m_{max} = 6$, and the maximum exponent of the radial function is 6. Note that due to the use of many local expansions, each with their own coefficients, the overall flexibility of the basis is much greater than what would be implied by these parameters if used as a single expansion.

To guide the placement of the high-level data—and avoid computing and discarding computationally expensive *ab initio* energies in highly repulsive regions—a lower-level guide PES was constructed using 2664 symmetry-unique points, distributed using a Sobol sequence[37] biased to sample the short range region more densely. For the construction of the high-level PES, initially, 1000 symmetry-unique points were distributed according to a Sobol sequence subject to an r_0-dependent bias—favoring points at $r_0 = 2.0$ Å over points at $r_0 = 15.0$ Å by a factor of about 20. Starting from these 1000 seed points, sets of 22 automatically determined points were added until the estimated global root-mean-square (RMS) fitting error was reduced to 1.0 cm^{-1}. The estimated error is computed from the differences between values obtained with the fitting basis with 301 functions and a basis that is one degree lower in both the radial basis (maximum radial power of 5) and the angular basis ($l_{max} = 5$, $m_{max} = 5$), for a total of 171 functions. Next, some additional *ab initio* data was included in the long range and the lowest energy regions. In total, 1756 symmetry-unique *ab initio* points were computed and used to fit the high-level PES. The final global RMS error is 0.05 cm^{-1} for energy-regions below the asympote. The analytical representation of the PES is available as Supporting Information (SI).

Table 1 Geometric parameters and potential energy for the global minimum (GM) and transition structures (TS) of the CO_2–N_2 complex. Units are Angströms, degrees, and cm^{-1}

	GM	TS1	TS2	TS3
R	3.685	4.456	3.205	3.393
θ_1	90.0	0.0	90.0	90.0
θ_2	0.0	90.0	90.0	90.0
φ_2	–	–	0.0	90.0
V	-323.0	-158.8	-107.1	-162.6

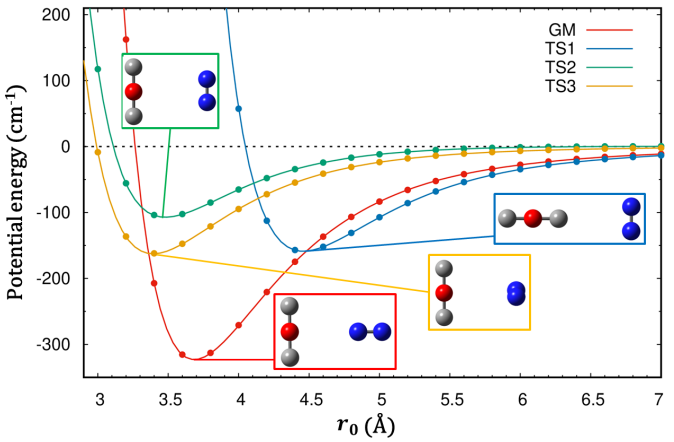

Fig. 3 The energy along various radial cuts defined by different relative orientations of the monomers is plotted, thus illustrating the significant anisotropy of the PES. The cuts through the global minimum (GM), and transition structure 1 (TS1), highlight the extent of relaxation of the intermonomer coordinate r_0 that occurs along the disrotatory energy path shown in Fig. 2. Lines represent the fitted PES, points represent *ab initio* calculations (not used in the fit).

2.3 Characterization of the PES

Fig. 2 shows a 2D representation of the PES (denoted r_0-optimized) for planar configurations, as a function of the extended angles $\tilde{\theta}_1$ and $\tilde{\theta}_2$. The position of stationary points and the corresponding molecular configurations of the system are also highlighted in the figure. The extended-angle coordinates have been described in detail elsewhere.[2] For planar geometries ($\varphi_2 = 0$ for quadrants II and IV, and $\varphi_2 = \pi$ for quadrants I and III), the plot describes the complete ranges of $\tilde{\theta}_1$ and $\tilde{\theta}_2$, relaxing the intermonomer distance coordinate r_0 for each pair of angles. This type of plot provides unique insight into the isomers in the system, since for many systems—those (such as this one) without non-planar minima—the plot will include all isomers and some relevant isomerization paths between them, making it easy to visualize planar motions during which φ_2 changes from 0 to π. There are two equivalent physical wells in the PES, each appearing twice in the extended angles plot, which shows four wells.

Our new PES, at the CCSD(T)-F12b/CBS level, is characterized by a single isomer corresponding to a T-shaped structure (labeled GM), with a well-depth of 323.0 cm^{-1}. The T-shape is formed by the N_2 molecule acting as a stem, pointing toward the C-atom of CO_2. The energies and geometric parameters of the global minimum and transition structures between equivalent minima are reported in Table 1. Fig. 3 shows 1D cuts of the potential as a function of r_0, upon approach towards the global minimum, and each of the other stationary points tabulated in Table 1.

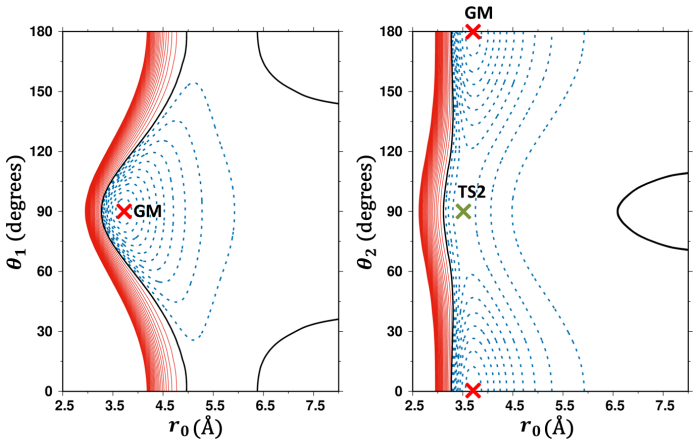

Fig. 4 2D cuts of the PES exploring the region around the global minimum for planar geometries (φ_2=0), holding the angle θ_2 (left panel) and θ_1 (right panel) fixed. Energies are in cm^{-1}. Red continuous lines represent positive energies (intervals of 60 cm^{-1}), the black line is the zero, and negative energies are represented by blue dashed contours (intervals of 30 cm^{-1}).

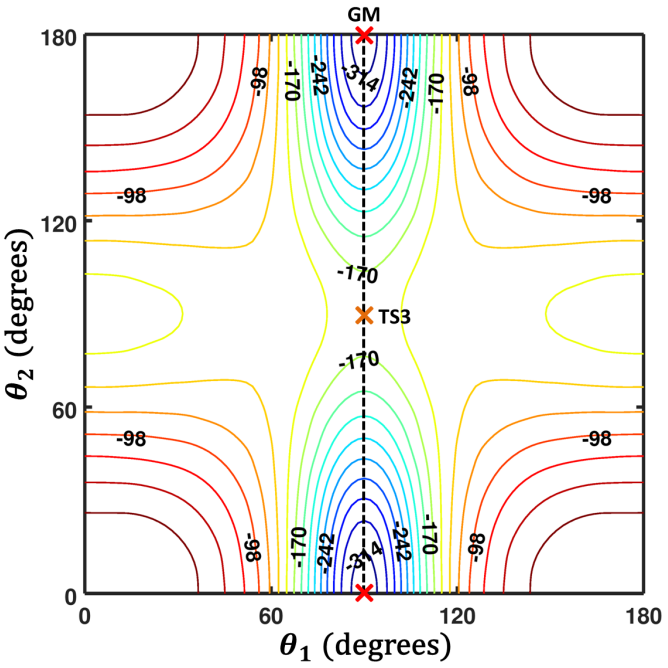

Fig. 5 2D cut of the PES as a function of θ_1 and θ_2, with $\varphi = 90$ degrees and r_0 equal to the value that minimizes the energy. The dashed line represents the out-of-plane path between equivalent minima.

The variation in those cuts gives some indication of the anisotropy of the interactions. In order to better appreciate the topography of the PES near the minimum, and the anisotropy of the interaction with respect to the CO_2 and N_2 rotations, additional 2D plots of the potential were made and are shown in Fig. 4. The plots in Fig. 4 explore the region around the minimum by presenting both the (r_0, θ_1) and (r_0, θ_2) planes that cross it.

Various motions of the monomers can move the system between symmetry equivalent wells on the PES. There are three paths between wells contributing to tunneling-splitting in the rovibrational states, which delocalize into the two wells. First, as indicated by the dashed line in Fig. 2, a disrotatory (or geared) motion moves the system along a planar low energy path between equivalent minima, passing through the transition structure 1 (TS1). The corresponding geared coordinate is $Q_g = (\tilde{\theta}_1 + \tilde{\theta}_2)/2$. A disrotatory path between minima is common in complexes formed by two linear monomers with planar minima. It is easily identified as it follows an angle of roughly 45 degrees from lower left to upper right in the extended angles plot (*cf.* Fig. 2). Some systems also (or instead) exhibit a conrotatory path; which is not seen here, but would connect minima by moving at roughly 45 degrees from lower right to upper left in the plot. Also in Fig. 2, a second planar path is seen, moving almost vertically between minima in the plot, passing through a much higher energy transition structure (TS2). This movement effectively flips the N_2 molecule while the CO_2 molecule relaxes slightly and then back again to $\theta_1 = 90$ degrees without flipping. A third out-of-plane path exists which is not visible on the extended angles plot—which only represents planar geometries—but is evident in Fig. 5, where a 2D cut of the PES is represented as a function of θ_1 and θ_2, with $\varphi = 90$ degrees and r_0 equal to the value that minimizes the energy for each set of angles. As the figure clearly shows, path three flips the N_2 molecule out-of-plane about its midpoint, passing through a cross-shaped transition structure (TS3). In some systems, a cross-like structure can appear as a minimum.[5] Fig. 6 compares paths 1 and 3. As can be seen in the figure, both paths involve similar barrier heights, with the barrier along the out-of-plane path being slightly lower (*cf.* Table 1). It is worth highlighting that all of the *ab initio* energies plotted in Fig. 3 and Fig. 6 were not used in the PES-construction process, and thus serve to confirm the overall quality of our fitted potential.

These characteristics are in slight contrast to the PES used in the previous study that we refer to as LSHH. The PES used in their study, reported in 2015 by Nasri *et al.*,[22] is based on data at the CCSD(T)-F12a/AVTZ level. They report a very similar global minimum, with a well depth of 321.2 cm^{-1}, but mention a second, less-stable isomer, corresponding to the other T–shaped structure (CO_2 pointing into N_2, our TS1). This structure, is reported as a tiny minimum, with a depth of only 0.8 cm^{-1}, located at the top of the disrotatory isomerization path between two equivalent global minimum structures. On our new PES,

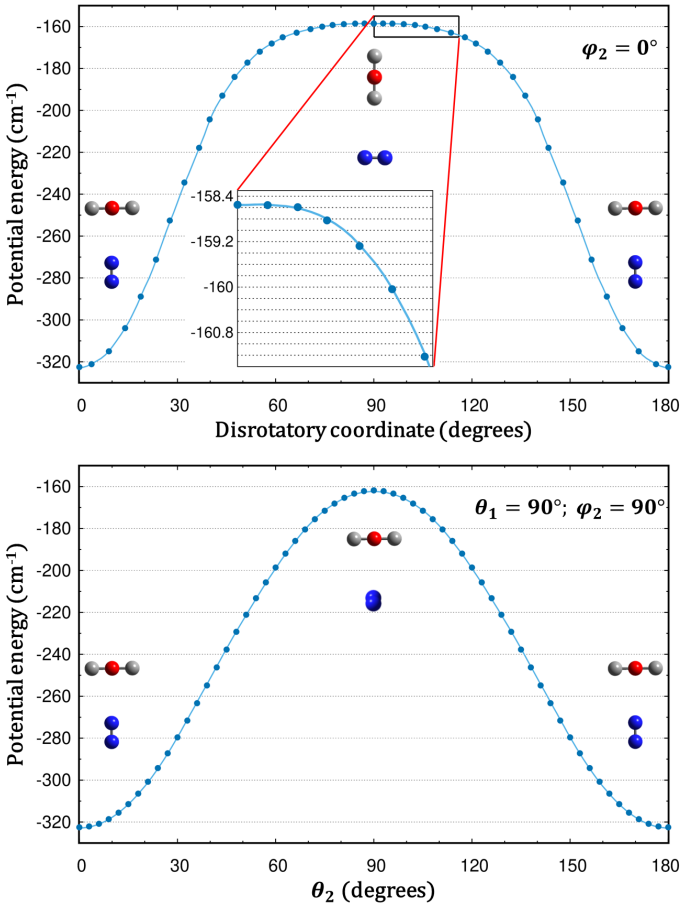

Fig. 6 (Upper) Energies along the planar minimum energy path between equivalent minima, shown in Fig. 2. Advancement of the disrotatory coordinate (set to zero at one minimum) tracks the geared motion of the monomers (see text). The inset highlights the absence of a second minimum near the top of the barrier. (Lower) Out-of-plane tumbling of the N_2 molecule represented by θ_2 carries the system over the lowest barrier to an equivalent minimum, as shown in Fig. 5. In all figures, lines represent the fitted PES, points represent *ab initio* calculations (not used in the fit).

no such minimum is found, but rather, we simply find a transition structure at this location at the top of the barrier along the path. The energies for angles approaching the top of the barrier are shown in the inset of the upper panel of Fig. 6. There are a few possible explanations for a tiny spurious minimum at this geometry. First, in general it could be an artifact of the fit, but in this case, it was reported as being present in the electronic structure data.[22] Then it is likely stemming either from finite basis set effects, or perhaps due to the F12a ansatz and the use of incomplete auxiliary bases, noting also that the system symmetry changes when arriving at a precisely T-shaped geometry, any of which can lead to small numerical issues. Nevertheless, in spite of the tiny additional minimum, the general behavior of the two PESs is quite similar, at least at the critical points. The energy at our TS1 is -158.8 cm^{-1}, almost exactly the same as the energy of the dip in their barrier, found at -158.9 cm^{-1}. The intermolecular separation at the minimum is $r_0 = 3.685$ Å.

3 Calculating Rovibrational Energies

To compute energy levels we use a spherical-harmonic type angular basis. Matrix elements of the kinetic energy operator are exact. Potential matrix elements are calculated with Gauss quadrature by doing sums sequentially.[38,39] Eigenvalues are obtained with the symmetry adapted Lanczos (SAL) algorithm.[40–42] Details are explained in previous papers.[6,43] Rovibrational levels have been computed with Lanczos methods for many years.[44–48] In addition to the vibrational coordinates of Fig. 1, we have Euler angles that specify the orientation of a body-fixed frame attached such that the z axis is along $\vec{r}_0$ and the x axis is along the vector $\vec{r}_0 \times \vec{r}_1 \times \vec{r}_0$. Masses of 14.0030740048, 12 and 15.9949146221 u were used for ^{14}N, ^{12}C and ^{16}O, respectively. Rotational constants for the monomers are: 0.39021894, and 1.98950 cm^{-1} for CO_2, and N_2 respectively.[1,29] As discussed above, the PES has a ceiling at 2 100 cm^{-1} above the separate monomers asymptote.

For the stretch coordinate basis we use a potential optimized discrete variable representation (PODVR)[49,50] with 50 functions defined in the range [3.78, 28.0] bohr and computed in a sine basis.[18,51] To test convergence we also computed levels using 20 and 80 PODVR, and 200 sine DVR functions. The results were found to be very well converged with respect to the radial basis. Energy level differences for larger radial bases, beginning at 20 PODVR functions, are less than 0.01 cm^{-1} for levels below -100 cm^{-1}. Max l_1, l_2, and m_2 quantum numbers for the angular basis are all 37, while 38 Gauss-Legendre quadrature points and 80 trapezoid points were used. Tests with angular bases as large as max l_1, l_2, and m_2 quantum numbers of 48, with 49 Gauss-Legendre quadrature points, and 97 trapezoid points were tested, and only tiny differences (less than 0.001 cm^{-1}) were noted beyond max l_1, l_2, and m_2 of 37. Most of our results were recorded using the basis of 50 PODVR functions and a max l_1, l_2, and m_2 of 37. This product-basis contains 2 960 200 functions.

To guide speculation about the bend frequency discrepancy in the LSHH results, we also explored the convergence obtained with much smaller angular bases. LSHH report using an angular basis with 15 CO_2 and 8 N_2 rotational states. They also mention using an energy-based truncation-diagonalization approach that could not be reproduced by our iterative Lanczos-based code, which retains the entire basis.

Table 2 Predicted (This work) and measured (Exp.) rotational transitions for the ground vibrational parent state, comparing the previously reported LSHH study with our new results. Transitions are given in MHz, percentage errors (% err.) are given with respect to the experimental values

Trans.	Exp.[54]	LSHH	% err.	This work	% err.
$1_{01}-0_{00}$	–	3880.484	–	3805.214	–
$2_{02}-1_{01}$	7608.377	7527.429	1.06	7602.542	0.08
$3_{03}-2_{02}$	11388.436	11277.417	0.98	11384.128	0.04
$4_{04}-3_{03}$	15148.195	15003.717	0.95	15142.260	0.04
$5_{05}-4_{04}$	18877.125	18698.230	0.95	18869.660	0.04

Table 3 Predicted (This work) and measured (Exp.) values for the four intermolecular vibrational mode band origins (in cm^{-1}), comparing predictions of the previous LSHH study with our new results

	This work	Exp.[23]	LSHH
GS	0.00	0.00	0.0
v_o	32.90	–	32.2
v_g	21.07	21.38[a]	45.9
v_s	46.51	–	46.3
v_a	59.46	–	51.2

[a] Measured for asymmetric stretch excited CO_2 monomer.

The molecular symmetry group[52] of the Hamiltonian is G_8, composed of the operations $\{E,\sigma_O,\sigma_N,\sigma_O\sigma_N\}\otimes\{E,E^*\}$. σ_O flips CO_2 (vector $\vec{r}_1$), σ_N flips N_2 (vector $\vec{r}_2$). There are eight irreducible representations which we label ee+, eo+, oe+, oo+, ee-, eo-, oe-, oo-, and $\pm$ label even and odd parities. e/o label states as symmetric or antisymmetric with respect to σ_O and σ_N, respectively. The point group for the equilibrium structure is C_{2v}. The point group is isomorphic to G_4, a sub-group of G_8 obtained by discarding σ_O and σ_N which are unfeasible because they require overcoming high barriers. All the levels are calculated using the G_8 group and have the G_8 irreducible representation (irrep) labels. To find the C_{2v} irreps, one can use the relation between the irreps of C_{2v} and those of the G_8. It is straightforward to separately calculate levels with even and odd parity by using a parity-adapted basis. The size of the even parity basis is 1 480 100. Within a parity block we calculate ee, eo, oe, and oo levels by using the SAL. The projection operators are easily obtained by knowing that basis functions are symmetric (anti-symmetric) with respect to permutation of the O atoms if l_1 is even (odd),[53] and symmetric (anti-symmetric) with respect to permutation of the N atoms in N_2 if l_2 is even (odd).[53] Since O is a spin-zero boson, only the rovibrational states that are symmetric with respect to the permutation of the O atoms are allowed, so ee+, eo+, ee- and eo- are allowed, while oe+, oo+, oe- and oo- are not.

4 Results and discussion

A series of rotational transitions—up to $J=5$ for the ground vibrational parent—were reported by LSHH and compared to the results of previous microwave experiments.[54] The computed transition energies were accurate to about 1 percent, which can be viewed as an affirmation of the quality of the PES, at least near the minimum. The absolute errors increased with J up to about 180 MHz at $J=5$, while remaining roughly constant in a relative (percentage) sense. With our improved PES, as shown in Table 2, we record absolute errors in our corresponding predictions in the range of 6-8 MHz, or 0.04 percent. This highlights the value obtained through the added cost of employing higher level electronic structure data. Had the calculation preceded the microwave measurements, predictions of this accuracy would actually be useful in guiding the setup and use of a high-sensitivity cavity-type spectrometer.

In Table 3 we list the transition frequencies for the four inter-molecular modes, compared with the results of LSHH and the new experimental measurement of v_g. In Table 4 we provide rotational constants derived from the $J=1$ levels and compare with available experimental values. Here, we label the four vdW modes as v_s, v_g, v_a, and v_o representing stretch, geared-bend, anti-geared-bend, and out-of-plane bend, respectively. LSHH number their mode labels, and label v_g as v_2. Mode v_g, on the ground state, is forbidden because its symmetry is oo+/oe+. The new experiment probed the combination band with CO_2 v_3 antisymmetric stretch vibration (whose symmetry is oe+) and the v_g inter-molecular mode. The total symmetry of this combination state is eo+/ee+ and therefore allowed. First, we note that our new prediction sides with the experimental measurement, with values of 21.07 cm^{-1} and 21.38 cm^{-1} for our new calculation and measurement respectively, compared with 45.9 cm^{-1} reported by LSHH previously. It is nice to settle the discrepancy and validate

Table 4 Rotational constants (in cm^{-1}) derived from $J=1$ levels are listed and compared with experimental values[23] where available*

	A	B	C
GS	0.396323	0.0687870	0.0581865
GS (Exp.)	0.396337(19)	0.0687903(23)	0.0581884(23)
v_o	0.407045	0.0695254	0.0613115
v_g	0.385177	0.0697742	0.0581362
v_g (Exp.)[a]	0.381576(29)	0.0696082(29)	0.0580675(28)
v_s	0.397979	0.0663190	0.0572853
v_a	0.402437	0.0693330	0.0569214

[a] Measured for asymmetric stretch excited CO_2 monomer.

* Experimental uncertainties (1σ) are in units of the last quoted digit.

the experiment, but looking at the results for the other three modes, it is not entirely obvious what the issue is with the LSHH results. The PES employed in their study is based on relatively high-level electronic structure data and the geometries and energies of the reported critical points are quite similar to ours (aside from the tiny secondary well, that is absent in ours). However, we do notice some peculiarities in their results, beginning with the PES. The disrotatory path plotted in Fig. 4 of LSHH appears quite different from ours (Fig. 6, upper panel), exhibiting a 'squeezed' minimum with an inflection above it, whereas ours appears as a simpler more open well. This coordinate more or less characterizes the ν_g mode in question. In addition, as noted by the authors, LSHH find nodes in their ground state wavefunction (see Figs. 3 and 5 of LSHH), whereas we do not (see our Fig. 7). They characterize the presence of nodes in a ground state wavefunction as uncommon, but speculate that they might be due to features of the PES, referred to as ripples and waves. In our experience, unphysical features of a PES will certainly perturb states and their energies, but not introduce nodes into the ground state wavefunction. We can not simply conclude that the levels are uniformly poorly converged either, since predictions for the other modes—especially ν_o and ν_s—are similar to ours. We did find that using a much smaller basis increased the frequency of ν_g significantly, but doing so also raised the energies of all the levels far above what is reported by LSHH, which for some of the levels seem pretty similar to ours (once the slight difference in well depths is accounted for).

In Table 5 we list the lowest ten levels in each symmetry block for $J = 0$. As discussed by LSHH, the allowed states are found in the two left-most columns (no 'double-prime-symmetry' states are allowed). The ground state is the first ee+ (A_1') state, which is symmetrically delocalized into the two equivalent wells (see Fig. 7, showing probability density in both wells). The anti-symmetric partner to the ground state, the lowest eo+ (B_2') state, raised slightly in energy by tunneling splitting. As discussed above, there are multiple tunneling paths available, the lowest barrier being some 67 cm^{-1} above the ground state. Due to the large masses and the high and wide barriers, not surprisingly, the ground state splitting is only 0.00009 cm^{-1}. The first oo+ (A_1'') and oe+ (B_2'') states are not allowed, but provide the band origin of the ν_g in-plane bending motion, found here at 21.07 cm^{-1} as discussed above and listed in Table 3. Being higher in energy, those states exhibit a slightly larger tunneling splitting of 0.00017 cm^{-1}. The pair of states for ν_s (stretch excited) are the third ee+ (A_1') and eo+ (B_2') states at 46.51 cm^{-1}, while the second states of oo+ (A_1'') and oe+ (B_2'') at 59.46 cm^{-1} correspond to excitation of ν_a (the high frequency in-plane bend). While the states corresponding to excitation of ν_s and ν_a are progressively higher in energy and the tunneling splittings are larger (0.00220 and 0.00113 cm^{-1} respectively), the splitting is actually larger for the lower of the two states, presumably due to a more favorable projection along a tunneling path. Indeed, the tunneling splitting for the pair of states oo- (A_2'') and oe- (B_1''), corresponding to excitation of the out-of-plane bending mode ν_o, is the largest of the fundamental modes, at 0.00441 cm^{-1}, despite those states being further below the barrier. In this case the excitation is directed along the lowest of the three tunneling paths. Of course, higher states with multiple quanta of excitation exhibit still larger splittings. A more complete list of state energies, including also $J > 0$, is given as Supporting Information.

Plots of wavefunctions or probability densities are useful to make assignments, as well as help to understand the role of features of the PES in guiding the (de)localization of states. LSHH reported states localized primarily in the region of a second minimum on their PES, despite it being located at the top of a barrier and having a depth of less than 1 cm^{-1}. As discussed above, in the construction

Table 5 Energies (in cm^{-1}) of the ten lowest levels in each symmetry block are listed for $J = 0$. The two left-most columns of energies are allowed states, while the two columns at right are not, but transitions involving ro-vibrational states whose vibrational parents do not exist are allowed (see text)

	ee+ (A_1')	eo+ (B_2')	oo+ (A_1'')	oe+ (B_2'')
1	0.000000	0.000091	21.071929	21.072101
2	41.317925	41.319152	59.458075	59.456941
3	46.505384	46.507580	61.664745	61.670445
4	63.272086	63.374153	72.322233	72.318839
5	75.139267	75.141738	83.840600	83.818142
6	80.338253	80.357066	89.027887	89.023433
7	87.661976	87.666029	97.370141	97.354952
8	93.058403	93.079845	98.725614	98.788135
9	100.088256	100.359145	107.718660	107.252517
10	100.533069	102.354698	111.566794	110.839126
	ee- (A_2')	eo- (B_1')	oo- (A_2'')	oe- (B_1'')
1	53.767358	53.768502	32.904777	32.909184
2	89.150214	89.124517	73.324550	73.362389
3	92.326983	92.390657	76.215733	76.320551
4	100.955510	100.757917	89.873607	91.032417
5	111.039198	110.516181	103.215262	103.371352
6	114.616625	113.883416	110.028356	110.441895
7	124.556853	119.930866	115.629022	115.846616
8	125.513320	123.922446	117.145061	120.585991
9	128.163274	127.425714	118.145490	122.743658
10	135.063791	130.551817	121.534187	127.179862

Energies are relative to the $ZPE = -229.461785$.

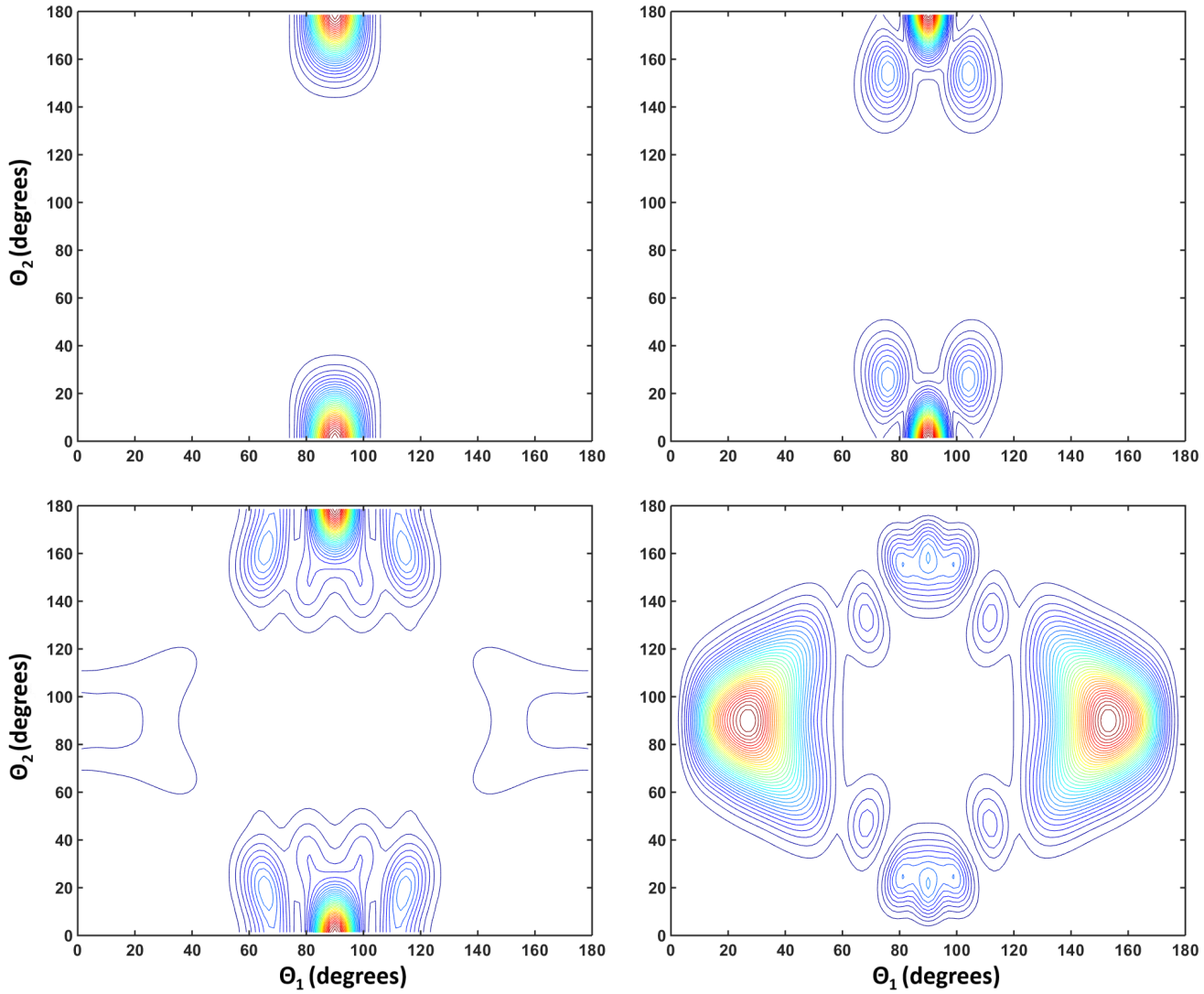

Fig. 7 The probability density is plotted for four states as a function of the angles θ_1 and θ_2, illustrating delocalization and possible nodes. The upper-left and upper-right panels show the first and second levels of ee+ (A_1') symmetry (the ground state and v_g 1st overtone respectively). The lower-left panel shows the 12th level of ee+ (A_1') symmetry, the lowest state with amplitude near the top of the interconversion path. The panel at lower-right shows an interesting state (the 9th level of oo- (A_2'') symmetry) exhibiting amplitude primarily located in the saddle region of the barrier.

of our new PES, we found that tiny minimum to be spurious and not to exist on our PES. Nevertheless, since it is questionable to what extent the tiny well was serving to confine the wavefunction to that region, we looked for states that might localize in that saddle region. Indeed, we do find some such states. The lowest energy state starting to show amplitude in that region is the 12th level of ee+ (A_1') symmetry ($E = 109.90$ cm^{-1}), also plotted in Fig. 7. However, that state is not primarily localized in that region, but rather is primarily located in the two global minimum wells, and exhibits a highly excited nodal pattern. This is much different than the nodeless amplitude typically found when a state is identified as the lowest one localized in a secondary minimum and classified as another isomer, as was reported by LSHH. We do not find such states in our results. Though not exhaustively, we looked at plots of various states in that energy range, and did finally encounter an interesting one that can be described as primarily localized in the saddle region (although highly excited and exhibiting a complex nodal pattern). It is the 9th state of oo- (A_2'') symmetry (not allowed, $E = 118.1$ cm^{-1}), and is also shown in Fig. 7. We see the character of states such as this one, not as a second isomer, but rather arising as a consequence of available energy, guidance by the topography of the PES, and constraints due to symmetry and orthogonalization with the other states.

5 Summary and conclusions

A discrepancy that recently came to light regarding rovibrational states of the atmospherically relevant CO_2–N_2 complex was investigated. New high-resolution spectroscopic measurements were found to differ significantly from recent high-level calculated predictions. The new experimental measurement was of the v_g, low frequency in-plane bending motion of the complex. A value of 21.4 cm^{-1} was extracted by analysis of combination bands, a poor match for the prediction of 45.9 cm^{-1}. This experimental procedure has been applied to many similar systems and serves as a good estimate of the ground state frequencies (typically within 0.1 cm^{-1}). On the other hand, previously recorded pure rotational transitions of the ground vibrational state of the complex were closely matched by the same set of calculations.

To address this, we constructed a new more accurate *ab initio* based PES describing the 4D intermolecular interactions between CO_2 and N_2, and used it to compute the low-lying rovibrational levels. Using iterative matrix algebra techniques it is straightforward to obtain highly converged results for states represented in a basis of millions of functions. Our results for v_g agree closely with the experimental measurement (21.1 cm^{-1} calculated vs. 21.4 cm^{-1} derived from the experiment). This level of agreement is about what is expected given the level of theory used to compute the PES, and the slight uncertainty in the experimental value, extracted from a combination band. We also compare our predictions for the rotational transitions of the ground vibrational state and note remarkably small errors, in the range of 6–8 MHz, which is sufficiently accurate to guide experimental measurements. Finally we note that a previously reported second isomer is not found on our PES, although states with interesting patterns of (de)localization were found by plotting probability densities.

Together, our automated PES-construction code AUTOSURF interfaced to our variational rovibrational code RV4, represent a highly efficient and effective tool for computational spectroscopy. Using parallel high-performance computing, it was possible to compute an accurate PES in less than a week. The rovibrational calculations are even quicker, but it takes some time and human expertise to compile and analyze the results.

Acknowledgments

We thank Nasser Moazzen-Ahmadi for drawing our attention to the differences between calculations and experimental measurements for this system. R.D. is supported by the US National Science Foundation (No. CHE-1566246). T.C. is supported by the Canadian Natural Sciences and Engineering Research Council.

Notes and references

1 J. Brown, X.-G. Wang, R. Dawes and T. Carrington Jr, *The Journal of Chemical Physics*, 2012, **136**, 134306.
2 R. Dawes, X. G. Wang and T. Carrington, *Journal of Physical Chemistry A*, 2013, **117**, 7612–7630.
3 X.-G. Wang, T. Carrington Jr and R. Dawes, *Journal of Molecular Spectroscopy*, 2016, **330**, 179–187.
4 E. Castro-Juárez, X.-G. Wang, T. Carrington Jr, E. Quintas-Sánchez and R. Dawes, *The Journal of chemical physics*, 2019, **151**, 084307.
5 J. Brown, X.-G. Wang, T. Carrington Jr, G. S. Grubbs and R. Dawes, *The Journal of Chemical Physics*, 2014, **140**, 114303.
6 R. Dawes, X.-G. Wang, A. W. Jasper and T. Carrington Jr, *The Journal of chemical physics*, 2010, **133**, 134304.
7 G. Donoghue, X.-G. Wang, R. Dawes and T. Carrington Jr, *Journal of Molecular Spectroscopy*, 2016, **330**, 170–178.
8 A. Barclay, A. McKellar, N. Moazzen-Ahmadi, R. Dawes, X.-G. Wang and T. Carrington, *Physical Chemistry Chemical Physics*, 2018, **20**, 14431–14440.
9 S. Sur, E. Quintas-Sánchez, S. A. Ndengué and R. Dawes, *Phys. Chem. Chem. Phys.*, 2019, **21**, 9168.
10 H. Cybulski, C. Henriksen, R. Dawes, X.-G. Wang, N. Bora, G. Avila, T. Carrington and B. Fernández, *Physical Chemistry Chemical Physics*, 2018, **20**, 12624–12636.
11 E. Quintas-Sánchez, R. Dawes, K. Lee and M. C. McCarthy, *The Journal of Physical Chemistry A*, 2020, 4445–4454.
12 E. Quintas-Sánchez and R. Dawes, *J. Chem. Inf. Model.*, 2019, **59**, 262–271.
13 X. Wang and T. Carrington Jr, *RV4 is a package of programs to compute rovibrational levels and wavefunctions of tetra-atomic molecules*, 2018.
14 X.-G. Wang and T. Carrington Jr, *The Journal of chemical physics*, 2002, **117**, 6923–6934.
15 X.-G. Wang, T. Carrington Jr, J. Tang and A. McKellar, *The Journal of chemical physics*, 2005, **123**, 034301.
16 S. Manzhos, X. Wang and T. Carrington Jr, *Chemical Physics*, 2018, **509**, 139–144.
17 J. Light, I. Hamilton and J. Lill, *The Journal of chemical physics*, 1985, **82**, 1400–1409.
18 J. C. Light and T. Carrington Jr, *Advances in Chemical Physics*, 2000, **114**, 263–310.
19 Z. Bačić and J. Light, *The Journal of chemical physics*, 1986, **85**, 4594–4604.

20 Z. Bačić and J. Light, *The Journal of chemical physics*, 1987, **86**, 3065–3077.

21 M. Lara-Moreno, T. Stoecklin, P. Halvick and M. Hochlaf, *Physical Chemistry Chemical Physics*, 2019, **21**, 3550–3557.

22 S. Nasri, Y. Ajili, N.-E. Jaidane, Y. N. Kalugina, P. Halvick, T. Stoecklin and M. Hochlaf, *The Journal of Chemical Physics*, 2015, **142**, 174301.

23 A. Barclay, A. McKellar and N. Moazzen-Ahmadi, *The Journal of Chemical Physics*, 2020, **153**, 014303.

24 M. C. McCarthy, S. A. Ndengué and R. Dawes, *The Journal of Chemical Physics*, 2018, **149**, 134308.

25 J.-P. Crusius, R. Hellmann, J. C. Castro-Palacio and V. Vesovic, *The Journal of chemical physics*, 2018, **148**, 214306.

26 G. Guelachvili, *Journal of Molecular Spectroscopy*, 1980, **79**, 72–83.

27 H. Li, P.-N. Roy and R. J. Le Roy, *The Journal of Chemical Physics*, 2010, **132**, 214309.

28 G. Guelachvili, *Journal of Molecular Spectroscopy*, 1980, **79**, 72–83.

29 R. Butcher, D. Willetts and W. Jones, *Proceedings of the Royal Society of London. A. Mathematical and Physical Sciences*, 1971, **324**, 231–245.

30 H. Werner, P. Knowles, G. Knizia, F. Manby, M. Schütz, P. Celani, W. Györffy, D. Kats, T. Korona, R. Lindh *et al.*, *MOLPRO, version 2019.1, a package of ab initio programs*, University College Cardiff Consultants Ltd.: Cardiff, UK, 2019.

31 H.-J. Werner, G. Knizia and F. R. Manby, *Molecular Physics*, 2011, **109**, 407–417.

32 D. Feller, K. A. Peterson and T. D. Crawford, *The Journal of chemical physics*, 2006, **124**, 054107.

33 B. Desrousseaux, E. Quintas-Sánchez, R. Dawes and F. Lique, *The Journal of Physical Chemistry A*, 2019, **123**, 9637–9643.

34 C. T. Bop, F. A. Batista-Romero, A. Faure, E. Quintas-Sánchez, R. Dawes and F. Lique, *ACS Earth and Space Chemistry*, 2019, **3**, 1151–1157.

35 R. Dawes and E. Quintas-Sánchez, *Reviews in Computational Chemistry vol. 31*, Wiley, 2018, ch. 5, pp. 199–264.

36 M. Majumder, S. A. Ndengue and R. Dawes, *Molecular Physics*, 2016, **114**, 1–18.

37 I. M. Sobol, *USSR Computational Mathematics and Mathematical Physics*, 1976, **16**, 236–242.

38 M. J. Bramley and T. Carrington Jr, *The Journal of chemical physics*, 1993, **99**, 8519–8541.

39 T. Carrington, *Canadian journal of chemistry*, 2004, **82**, 900–914.

40 X.-G. Wang and T. Carrington Jr, *The Journal of Chemical Physics*, 2001, **114**, 1473–1477.

41 R. Chen and H. Guo, *The Journal of Chemical Physics*, 2001, **114**, 1467–1472.

42 X.-G. Wang and T. Carrington Jr, *The Journal of Chemical Physics*, 2001, **115**, 9781–9796.

43 X.-G. Wang, T. Carrington Jr, R. Dawes and A. W. Jasper, *Journal of Molecular Spectroscopy*, 2011, **268**, 53–65.

44 P. Sarkar, N. Poulin and T. Carrington Jr, *The Journal of chemical physics*, 1999, **110**, 10269–10274.

45 S. Y. Lin and H. Guo, *The Journal of chemical physics*, 2003, **119**, 5867–5873.

46 H.-G. Yu, H. Song and M. Yang, *The Journal of Chemical Physics*, 2017, **146**, 224307.

47 A. McNichols and T. Carrington Jr, *Chemical physics letters*, 1993, **202**, 464–470.

48 C. Iung and C. Leforestier, *The Journal of Chemical Physics*, 1989, **90**, 3198–3203.

49 H. Wei and T. Carrington Jr, *The Journal of chemical physics*, 1992, **97**, 3029–3037.

50 J. Echave and D. C. Clary, *Chemical physics letters*, 1992, **190**, 225–230.

51 C. Leforestier, *The Journal of chemical physics*, 1991, **94**, 6388–6397.

52 P. R. Bunker and P. Jensen, *Molecular symmetry and spectroscopy*, NRC Research Press, 2006.

53 X.-G. Wang and T. Carrington, *The Journal of Physical Chemistry A*, 2007, **111**, 10220–10225.

54 D. J. Frohman, E. S. Contreras, R. S. Firestone, S. E. Novick and W. Klemperer, *The Journal of chemical physics*, 2010, **133**, 244303.

A new potential energy surface for the atmospherically relevant CO_2-N_2 complex was constructed and used to compute rovibrational levels

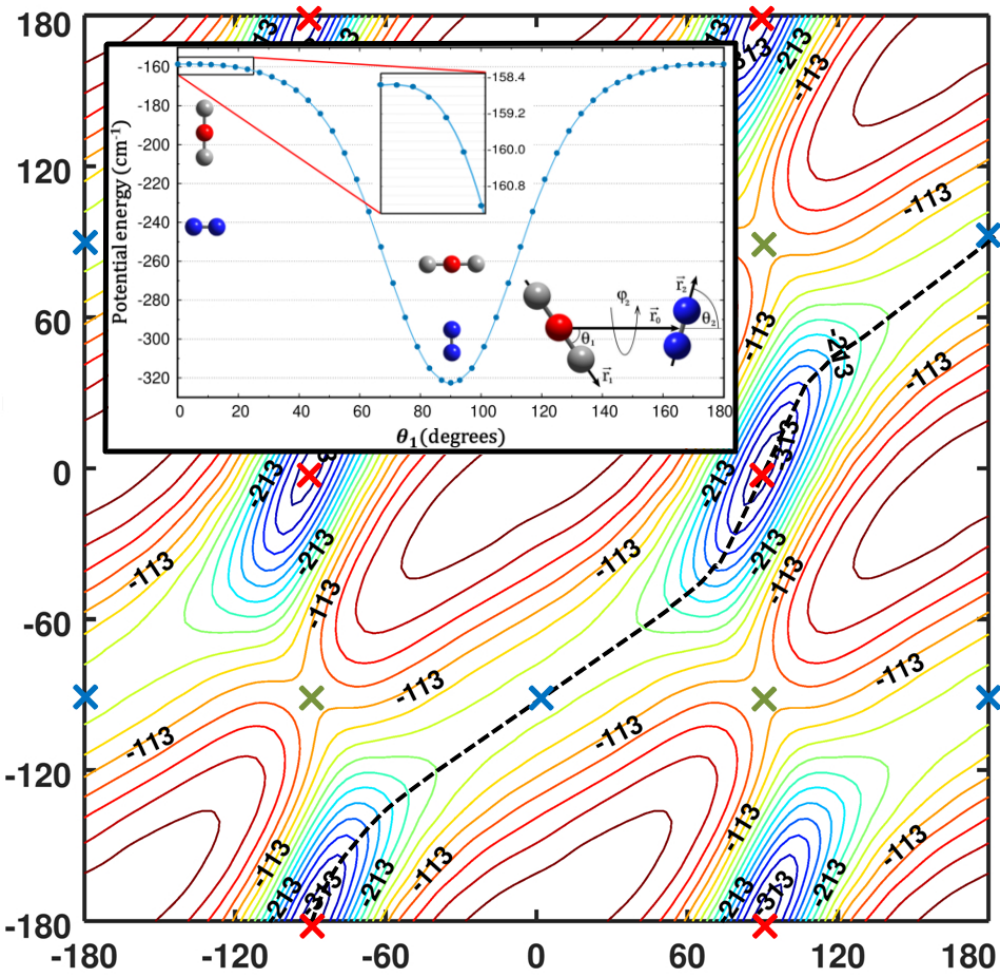
180
120
60
0
-60
-120
-180
-180
-120
-60
0
60
120
180
-113
-213
-313
Potential energy (cm-1)
-160
-180
-200
-220
-240
-260
-280
-300
-320
0
20
40
60
80
100
120
140
160
180
θ1 (degrees)
-158.4
-159.2
-160.0
-160.8